PET Imaging Evaluation of Four σ_1 Radiotracers in Nonhuman Primates

Evan Baum[1], Zhengxin Cai[1], Frederic Bois[1], Daniel Holden[1], Shu-fei Lin[1], Teresa Lara-Jaime[1], Michael Kapinos[1], Yuanyuan Chen[2], Winnie Deuther-Conrad[3], Steffen Fischer[3], Sladjana Dukic-Stefanovic[3], Paul Bunse[4], Bernhard Wünsch[4], Peter Brust[3], Hongmei Jia[2], and Yiyun Huang[1]

[1]PET Center, Department of Radiology and Biomedical Imaging, Yale University, New Haven, Connecticut; [2]Ministry of Education Key Laboratory of Radiopharmaceuticals, College of Chemistry, Beijing Normal University, Beijing, China; [3]Helmholtz-Zentrum Dresden-Rossendorf, Institute of Radiopharmaceutical Cancer Research, Leipzig, Germany; and [4]Department of Pharmaceutical and Medicinal Chemistry, Westfälische Wilhelms-Universität Münster, Münster, Germany

The σ_1 receptors (S1Rs) are implicated in a variety of diseases including Alzheimer disease and cancer. Previous PET S1R radiotracers are characterized by slow kinetics or off-target binding that impedes their use in humans. Here, we report the first PET imaging evaluation in rhesus monkeys of 4 ^{18}F-labeled spirocyclic piperidine-based PET radiotracers (^{18}F-**1** to ^{18}F-**4**). **Methods:** Baseline scans for the 4 radiotracers were obtained on an adult male rhesus monkey. Blocking scans were obtained with the S1R-selective agonist SA4503 to assess binding specificity of ^{18}F-**2** and ^{18}F-**4**. Arterial input functions were measured, and binding parameters were determined with kinetic modeling analysis. **Results:** In the rhesus brain, all 4 radiotracers showed high and fast uptake. Tissue activity washout was rapid for ^{18}F-**2** and ^{18}F-**4**, and much slower for ^{18}F-**1** and ^{18}F-**3**, in line with their respective in vitro S1R-binding affinities. Both the 1-tissue-compartment and multilinear analysis-1 kinetic models provided good fits of time–activity curves and reliable estimates of distribution volume. Regional distribution volume values were highest in the cingulate cortex and lowest in the thalamus for all radiotracers. ^{18}F-**4** showed greater differential uptake across brain regions and 3-fold-higher binding potential than ^{18}F-**2**. SA4503 at the dose of 0.5 mg/kg blocked approximately 85% (^{18}F-**2**) and 95% (^{18}F-**4**) of radiotracer binding. **Conclusion:** Tracers ^{18}F-**2** and ^{18}F-**4** displayed high brain uptake and fast tissue kinetics, with ^{18}F-**4** having higher specific binding signals than ^{18}F-**2** in the same monkey. Taken together, these data indicate that both ^{18}F-**2** and ^{18}F-**4** possess the requisite kinetic and imaging properties as viable PET tracers for imaging S1R in the human brain.

Key Words: sigma-1 receptor; PET; radioligand; ^{18}F; rhesus monkey

J Nucl Med 2017; 58:982–988
DOI: 10.2967/jnumed.116.188052

The σ_1 receptors (S1Rs) are chaperone proteins localized at mitochondrial associated endoplasmic reticulum membranes that have been shown to play a role in a wide range of diseases, including addiction, amnesia, Alzheimer disease, amyotrophic lateral sclerosis, and cancer (*1,2*). Several studies have detailed the roles of S1R in regulating potassium channels, neuritogenesis, calcium signaling, memory, and drug addiction (*3–5*). A variety of psychoactive chemicals and neurosteroids have been shown to interact with S1R, including haloperidol, (+)-*N*-allylnormetazocine (SKF-10,047), cocaine, and progesterone (*6–8*). Maurice et al. (*9*) demonstrated that the S1R agonists (+)-pentazocine, PRE-084, and SA4503 exhibit antiamnesia effects in a dose-dependent manner in mice with β_{25-35} amyloid–induced amnesia. These results demonstrate a link between S1R and the pathologic states affecting the cholinergic and glutamatergic systems, which may be of therapeutic importance in the process of aging (*9*).

Given the diverse interactions of S1R in pathophysiology, a PET imaging agent for use in humans would allow for the noninvasive investigation of S1R in vivo and lead to new understandings of its function and dysfunction in disease states. It will also make it possible to correlate and translate preclinical findings in animal models to humans and help in the development of novel therapeutic agents.

Several PET radioligands for S1R have been developed, including ^{18}F-FPS, ^{18}F-FBP, ^{18}F-FTC-146, and ^{11}C-SA4503 (Fig. 1) (*10–13*). An ideal tracer would possess appropriate affinity; high selectivity for S1R versus S2R and the vesicular acetylcholine transporter (VAChT); and fast, reversible tissue kinetics. Furthermore, it should have the requisite lipophilicity (Log D = 1–3) to cross the blood–brain barrier (*14*). (*R*)-(+) and (*S*)-(–)-^{18}F-fluspidine (^{18}F-**1** and ^{18}F-**2**, respectively) demonstrated good S1R binding affinity and favorable kinetics when tested in rodents and pigs (*15–17*). Kranz et al. (*18*) also evaluated ^{18}F-**2** in 4 healthy human subjects for dosimetry calculations. Li et al. (*14*) described a series of spirocyclic piperidine derivatives with subnanomolar affinity for S1R and greater than 100-fold selectivity over S2R and VAChT, including ^{18}F-1′-(4-fluoroethoxy)benzyl)-3H-spiro[2-benzofuran-1,4′-piperidine] (^{18}F-**3**). In a subsequent paper, Chen et al. (*19*) reported the synthesis and evaluation of ^{18}F-1′-((6-(2-fluoroethoxy)pyridin-3-yl)methyl)-3H-spiro[2-benzofuran-1,4′-piperidine] (^{18}F-**4**) in mice. Faster clearance and greater specific binding was observed for the *N*-pyridinyl analog ^{18}F-**4** than the *N*-benzyl analog ^{18}F-**3**. The spirocyclic piperidine series thus demonstrated promising properties to image S1R with PET based on their high selectivity toward S1R and good binding characteristics in rodents, pigs, and a preliminary human study (*14,16–19*). Here, we report the first PET imaging evaluation in nonhuman primates of 4 radioligands (^{18}F-**1** through ^{18}F-**4**, Fig. 1) from this

Received Dec. 8, 2016; revision accepted Feb. 9, 2017.
For correspondence or reprints contact: Yiyun (Henry) Huang, Yale PET Center, 801 Howard Ave., New Haven, CT 06520-8048.
E-mail: henry.huang@yale.edu
Published online Feb. 23, 2017.

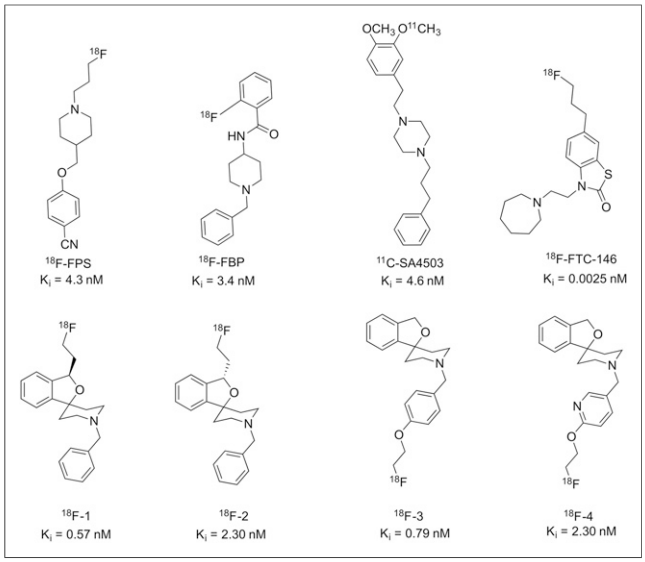

FIGURE 1. Structures of previous S1R tracers ^{18}F-FPS, ^{18}F-FBP, ^{11}C-SA4503, and ^{18}F-FTC-146, and spirocyclic piperidine derivatives ^{18}F-**1** to ^{18}F-**4**, with in vitro K_i values for S1R (*10–15*).

series to assess their pharmacokinetics and in vivo binding properties, and to select the most suitable tracer for advancing to evaluation in humans.

MATERIALS AND METHODS

Chemistry

Precursors and reference standards for ^{18}F-**1** and ^{18}F-**2** were prepared at Westfälische Wilhelms-Universität Münster, as previously reported (*15*). Precursors and standards for ^{18}F-**3** and ^{18}F-**4** were synthesized at Beijing Normal University (*14*).

Radiochemistry

Instrumentation for radiochemistry procedures and the production of ^{18}F-fluoride have been described previously (*20,21*). Radiosynthesis of ^{18}F-**1** to ^{18}F-**3** was achieved via nucleophilic displacement of the corresponding tosylate precursors (**5–7**, Fig. 2) with $^{18}F^-$ in the presence of Kyrptofix 2.2.2 and potassium carbonate (*14,15*). ^{18}F-**4** was prepared in a 2-pot, 2-step synthesis, first isolating ^{18}F-fluoroethyl tosylate followed by its reaction with the 2-pyridinol precursor (**8**, Fig. 2) (*19,22*). Chemical purity, radiochemical purity, and specific activity were determined by high-performance liquid chromatography analysis of the final product solutions. Identities of the labeled compounds were confirmed by coinjection of the products with their respective unlabeled reference standards.

PET Imaging Experiments in Rhesus Monkeys

PET Procedures. Experiments were performed in rhesus monkeys (*Macaca mulatta*) according to procedures approved by the Yale University Institutional Animal Care and Use Committee and described previously (*20*).

Three animals were used in this study. The animals were immobilized with ketamine (10 mg/kg intramuscularly) and anesthetized with 1.5%–2.5% isoflurane. An arterial line was placed in the radial or femoral artery for blood sampling. Scans were acquired on a FOCUS 220 camera (Siemens Medical Solutions). Before radioligand injection, a 9-min transmission scan was obtained for attenuation correction. Baseline scans were obtained over 4 h on a 7-y-old male rhesus monkey (13.8 kg). Each tracer was injected intravenously over 3 min as a slow bolus (~185 MBq in 10 mL). Two-hour blocking scans of ^{18}F-**2** and ^{18}F-**4** were acquired with a dose of SA4503 (0.5 mg/kg) (*6*) given intravenously 10 min before radioligand administration. Two additional baseline scans were obtained for ^{18}F-**2** and ^{18}F-**4** on a 12-y-old female (6.1 kg) and a 9-y-old female (9.7 kg) monkey, respectively, for comparison with baseline scans obtained in the 7-y-old male. Eight PET scans were obtained in total.

Metabolite Analysis and Arterial Input Function Measurement. Procedures for measurement of the arterial input function, including sample preparation, metabolite analysis, and data processing, have been described previously (*20*). Arterial samples were collected at preselected time points, and the radioactivity concentrations in the whole blood and plasma were measured. During the 4-h baseline scans, samples at 3, 8, 15, 30, 60, 90, 120, 180, and 240 min (3, 8, 15, 30, 60, 90, and 120 min for the 2-h scans) after injection were processed and analyzed by high-performance liquid chromatography using a modified column-switching system (*23*) to determine the fraction of unmetabolized tracer over the course of the scan. A biexponential function was fitted to the measured parent fractions to produce a continuous function describing the parent fraction over time. The input function was calculated as the product of the total plasma activity and interpolated parent fraction at each time point. The measured input function values were fitted to a sum of 3 exponentials, and the fitted values were used as inputs for kinetic analyses.

Plasma Free Fraction (f_P) and Log D Measurement. The f_P was measured via ultrafiltration of 0.3-mL aliquots of plasma spiked with a small amount (~740 kBq) of radioligand, repeated in triplicate. The amount of radioactivity in the filter and filtrate was counted and f_P calculated as the ratio of the concentration (radioactivity/mL) of the filtrate to the total activity. The log *D* of each tracer was determined by the shake-flask method as described previously (*24*).

Image Analysis and Kinetic Modeling. Procedures for PET image reconstruction, definition of regions of interest (ROIs), and kinetic analysis have been detailed previously (*20*). Emission data were attenuation corrected using the transmission scan, and dynamic images (33 frames over 120 min or 57 frames over 240 min) were reconstructed using a filtered backprojected algorithm with a Shepp-Logan filter. ROIs were defined from a single representative anatomic rhesus MR image registered to a template image. Registration parameters were derived to apply ROIs to each PET scan, and time–activity curves were generated for the following 16 cortical and subcortical brain regions: amygdala, brain stem, caudate, cerebellum, cingulate cortex, frontal cortex, globus pallidus, hippocampus, insula, nucleus accumbens, occipital cortex, pons, putamen, substantia nigra, temporal cortex, and thalamus.

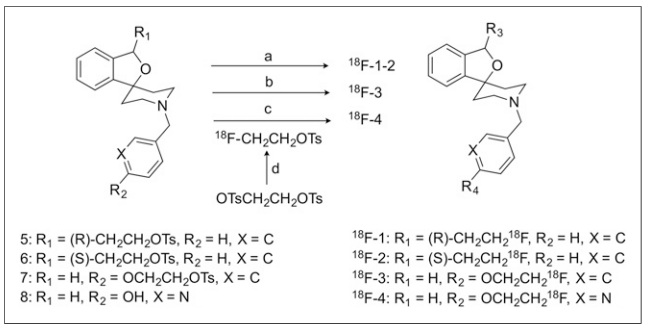

FIGURE 2. Syntheses of the 4 radiotracers. Reagents and conditions: (a) $^{18}F^-$, Kryptofix 2.2.2, K_2CO_3, MeCN, 85°C, 20 min; (b) $^{18}F^-$, Kryptofix 2.2.2, K_2CO_3, MeCN, 95°C, 20 min; (c) $^{18}F^-$, Kryptofix 2.2.2, K_2CO_3, MeCN, 80°C, 10 min; and (d) Cs_2CO_3, DMF, 110°C, 10 min.

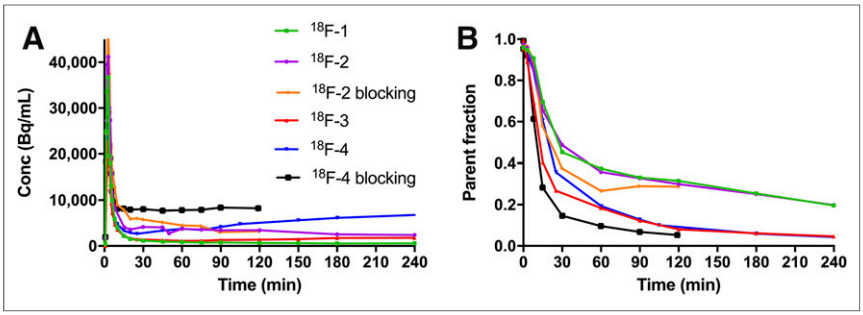

FIGURE 3. Plasma analysis of the 4 radiotracers in the same monkey. (A) Total radioactivity in plasma over time. (B) Time course of parent fraction from 4-h baseline and 2-h blocking scans with SA4503.

Regional volumes of distribution (V_T, mL·cm^{-3}) were determined by kinetic analysis of the time–activity curves, using the metabolite-corrected arterial plasma input function according to 1-tissue- and 2-tissue-compartment (1TC and 2TC, respectively) models and the multilinear analysis-1 (MA1) method as described previously (*25,26*). Standard errors in V_T estimates from different models were compared to determine the optimal model for analysis.

Comparison of V_T between tracers was used to determine the relative regional nondisplaceable binding potential (BP_{ND}) by graphical methods (*27*). In this analysis, V_T^A of one tracer is plotted on the *x*-axis and V_T^B of another is plotted on the *y*-axis. A linear regression yields the following equation:

$$V_T^B = \frac{f_p^B}{f_p^A}\frac{K_D^A}{K_D^B}V_T^A + V_{ND}^B\left(1 - \frac{BP_{ND}^B}{BP_{ND}^A}\right). \quad \text{Eq. 1}$$

More negative values for the *y*-intercept indicate $BP_{ND}^B > BP_{ND}^A$ and vice versa. Because f_P was measured for all tracers, the ratio of equilibrium dissociation constants (K_D) between the tracers can be determined from the slope of the regression (*27*).

S1R occupancies with SA4503 were calculated using V_T values from all 16 ROIs to create occupancy plots according to the method of Cunningham et al. (*28*). For ^{18}F-**2** and ^{18}F-**4**, regional BP_{ND} values were calculated using the nondisplaceable volume of distribution (V_{ND}) obtained from the occupancy studies, where $BP_{ND} = (V_T/V_{ND}) - 1$ (*26*).

RESULTS

Radiochemistry

All tracers were synthesized in greater than 96% radiochemical purity and high specific activity (349.4 GBq/μmol average at the end of synthesis, $n = 7$). Total synthesis time was 110 ± 30 min. Radiochemical yields (±SD where applicable) were 2.0%, 6.2% ± 1.7% ($n = 2$), 0.66%, and 6.5% ± 9.2% ($n = 3$), respectively, for ^{18}F-**1**, ^{18}F-**2**, ^{18}F-**3**, and ^{18}F-**4**.

TABLE 1
Comparison of K_i, Selectivity, Lipophilicity, and f_P

Ligand	K_i (σ-1)	K_i (σ-2)	Selectivity	Log *D*	f_P
^{18}F-**1**	0.57 nM*	1,650 nM*	2,895*	2.8	2%
^{18}F-**2**	2.3 nM*	897 nM*	390*	2.8	2%
^{18}F-**3**	0.79 nM†	277 nM†	351†	2.55	8%
^{18}F-**4**	2.3 nM†	327 nM†	142†	2.5	18%

*Taken from Holl et al. (*15*).
†Taken from Li et al. (*14*).

In Vivo Evaluation in Rhesus Monkeys

After a bolus injection of the tracers (179.8 ± 12.8 MBq; specific activity, 315.3 GBq/μmol average at time of injection; injected mass, 0.34 ± 0.25 μg; $n = 6$), total plasma activity and parent activity exhibited a rapid rise and clearance, followed by a stabilization or slow decrease over time for ^{18}F-**1** to ^{18}F-**3**, and a slight increase for ^{18}F-**4** (Fig. 3A). Metabolism rates were moderate, with 37%, 35%, 18%, and 19% of parent fraction, respectively, for ^{18}F-**1**, ^{18}F-**2**, ^{18}F-**3**, and ^{18}F-**4** at 60 min after injection (Fig. 3B). Blocking with SA4503 increased plasma activity particularly for ^{18}F-**4** (Fig. 3A) and increased metabolism for ^{18}F-**2** and ^{18}F-**4** (Fig. 3B). Typical metabolite profiles over time under baseline conditions are presented in Supplemental Figures 1–4 (supplemental materials are available at http://jnm.snmjournals.org). Polar metabolites have been previously suggested for these tracers that should not enter the brain and interfere with PET quantitation (*14,15,17*).

Plasma f_P values were measured at 2%, 2%, 8%, and 17%, respectively, for ^{18}F-**1**, ^{18}F-**2**, ^{18}F-**3**, and ^{18}F-**4**, consistent with their respective measured Log *D* values of 2.80, 2.80, 2.55, and 2.50. A summary of in vitro K_i, f_P, and Log *D* values are shown in Table 1.

Regional time–activity curves (Fig. 4) were generated and analyzed with 1TC and 2TC models (*26*), as well as the MA1 method (*25*) using the metabolite-corrected arterial plasma input function. The 1TC model was found to provide better fits than the 2TC model, with the 2TC model producing high SEs in V_T estimates across many regions (e.g., >20% SE in 28% of regions under all conditions, and >150% SE in 75% of regions for ^{18}F-**4** under blocking condition). Therefore, the 1TC would be considered an appropriate model for analysis of imaging data. Regional V_T values estimated by MA1 showed good correlation with 1TC values (e.g., for ^{18}F-**4**, $V_{T\ (MA1)} = 0.975\ V_{T\ (1TC)} + 1.239$, $r^2 = 0.996$). Listed in Table 2 are the 1TC-derived V_T values for the tracers across brain regions, under both baseline and blocking conditions. The time stability of V_T values was also determined for the 4 tracers, revealing bias and regional errors associated with shorter scan times (Fig. 5).

Blocking with SA4503 reduced V_T values for ^{18}F-**2** and ^{18}F-**4** in all brain regions, indicating the lack of a suitable reference region for S1R in monkey (Table 2). Receptor occupancies by 0.5 mg/kg SA4503 were 85% and 95% for ^{18}F-**2** and ^{18}F-**4**, respectively (Supplemental Fig. 5). Values of V_{ND} were calculated for ^{18}F-**2** and ^{18}F-**4** from the occupancy plots using 1TC- and MA1-derived V_T values (*28*), yielding $V_{ND\ (1TC)} = 6.87$ and $V_{ND\ (MA1)} = 7.30$ for ^{18}F-**2** and $V_{ND\ (1TC)} = 9.29$ and $V_{ND\ (MA1)} = 10.44$ for ^{18}F-**4**. These values were then used to calculate the BP_{ND}, as a measure of specific binding signal, across the brain regions (Table 3). Relative BP_{ND} and K_D for all tracers were also assessed by the graphical methods of Guo et al. (*27*) by comparing baseline V_T values, which showed a rank order of

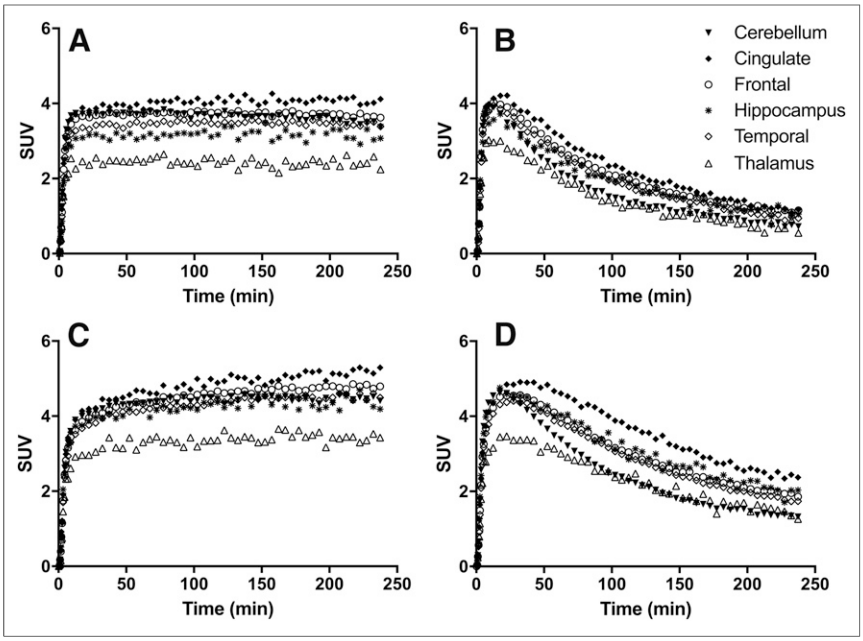

FIGURE 4. Time–activity curves of ^{18}F-**1** (A), ^{18}F-**2** (B), ^{18}F-**3** (C), and ^{18}F-**4** (D) in selected brain regions from baseline scans in the same monkey. For clarity of presentation, not all brain regions are displayed.

^{18}F-**3** > ^{18}F-**1** > ^{18}F-**4** > ^{18}F-**2** for BP_{ND} and ^{18}F-**4** > ^{18}F-**2** > ^{18}F-**1** > ^{18}F-**3** for K_D.

DISCUSSION

In this article, we describe the evaluation of 4 ^{18}F-labeled S1R tracers in nonhuman primates to compare their pharmacokinetic and binding characteristics and assess feasibility for use in human subjects.

In the rhesus monkey brain, all 4 tracers demonstrated high uptake, as shown in time–activity curves presented in Figures 4A–4D. Activity peaked between 10 and 20 min after injection, indicating fast uptake kinetics. Fast tracer washout was observed for ^{18}F-**2** and ^{18}F-**4**, with much slower washout for ^{18}F-**1** and ^{18}F-**3**. Time–activity curves depict ^{18}F-**4** as having the most heterogeneous uptake across brain regions, further displayed in summed images of the adult male monkey (Figs. 6A–6D). For all tracers, uptake was highest in the cingulate cortex, insula, and frontal cortex; intermediate in the hippocampus, temporal, and occipital cortices; and lowest in the caudate and thalamus (Figs. 4A–4D). Although this distribution pattern is in agreement with results from an in vivo imaging study with ^{11}C-SA4503 and in vitro autoradiography study with (+)-^{3}H-3-PPP in rhesus monkey brains (*29,30*), it differs somewhat from ex vivo autoradiography studies with ^{18}F-**3** and ^{18}F-**4** in rats (*14,19*), which showed high accumulation in the temporal cortex, frontal cortex, and vermian lobule of the cerebellum; moderate uptake in the hippocampus, hypothalamus, and thalamus; and low accumulation in the nucleus accumbens. Studies with ^{18}F-fluspidine in mice (*16*) showed the highest uptake in the facial nucleus, moderate uptake in the cerebellum, and low binding in the thalamus and caudate/putamen. PET imaging studies using ^{18}F-**1** and ^{18}F-**2** in pigs (*17*) demonstrated narrow regional differences, with the highest uptake in the midbrain, pons, and thalamus; moderate uptake in the hippocampus and temporal and occipital cortices; and lowest uptake in the frontal cortex. The distribution patterns of these 4 tracers in monkeys also align well with that of ^{11}C-SA4503 in humans (*31*), with high uptake in cortical and limbic areas and lower uptake in caudate, putamen, and thalamus. Species differences in tracer uptake between rodents, pigs, and primates highlight the importance of tracer evaluation in nonhuman primates before translation to humans.

TABLE 2
Comparison of 1TC-Derived V_T Values for the 4 Tracers Across Different Brain Regions

	V_T (mL•cm^{-3})									
Condition	Amygdala	Caudate	Cerebellum	Cingulate cortex	Frontal cortex	Hippocampus	Occipital cortex	Putamen	Temporal cortex	Thalamus
^{18}F-**1** baseline	152.8	180.8	174.9	291.4	215.5	192.8	174.1	199	215.7	127.7
^{18}F-**2** baseline	14.6 (31.6)*	13.5 (28.4)*	13.6 (30.2)*	19.6 (37.9)*	17.8 (35.1)*	16.4 (33.5)*	14.6 (30.0)*	14.9 (31.8)*	16.5 (32.6)*	12.2 (30.2)*
^{18}F-**3** baseline	574.9	479.3	507.8	1351.9	1099.7	575.8	786.9	530.3	916.8	471
^{18}F-**4** baseline	44.4 (42.3)*	36.7 (35.7)*	35.3 (32.7)*	57.9 (56.8)*	46.5 (47.6)*	48.2 (46.5)*	38.2 (31.7)*	38.1 (35.9)*	44.4 (40.6)*	35.3 (38.9)*
^{18}F-**2** SA4503 block	6.2	7.1	7.6	8.6	8.3	7.5	8	8.8	8.3	7.2
^{18}F-**4** SA4503 block	9.4	10.3	9.9	12	11.9	9.8	10.8	11.9	11.5	9.8

*Baseline V_T values in 2 different female monkeys are noted in parentheses for ^{18}F-**2** and ^{18}F-**4**.

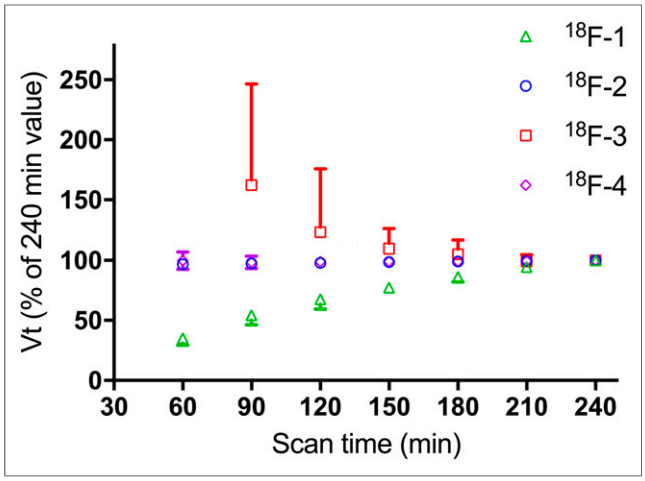

FIGURE 5. Time stability of V_T for the 4 tracers. Times refer to midtimes of each 10-min acquisition. Data from 60 to 240 min were analyzed in 30-min increments, and V_T expressed as percentage of value derived with complete dataset (240 min). Each point is average V_T from 16 ROIs. Deviation from 100% of mean value indicates bias associated with shorter scanning times, whereas SD indicates regional error associated with shorter scanning times. Bias and error for ^{18}F-**3** at 60 min was too large (>10,000%) to display.

Regional V_T values appear to be sex-independent because a comparison baseline scan for ^{18}F-**4** in a 9-y-old female rhesus monkey gave numbers similar to those from the 7-y-old male (Table 2). However, the baseline V_T values obtained with ^{18}F-**2** in the 12-y-old female were higher than those from the 7-y-old male, which could be due to individual animal variation in S1R expression, or age effect, as Matsuno et al. reported increased S1R density in aged rhesus monkeys (*29*).

A comparison of V_T estimates versus scan time demonstrated the bias and regional error associated with shorter scan times (Fig. 5). With 60 min of scan data, V_T values for both ^{18}F-**2** and ^{18}F-**4** were within 10% difference of those derived from the full 240 min data, and within 5% difference when estimated with 90 min of scan data. Tracers ^{18}F-**1** and ^{18}F-**3** demonstrated much larger bias and greater errors with shorter scan times, only approaching within 5% difference from the 240-min V_T values at 210 min of scanning time. V_T values for ^{18}F-**1** were underestimated whereas those of ^{18}F-**3** were overestimated with shorter acquisition times (Fig. 5). For these reasons, ^{18}F-**2** and ^{18}F-**4** gave reliable V_T estimates at 90 min, whereas ^{18}F-**1** and ^{18}F-**3** required much longer scan times.

On the basis of their extremely slow tissue kinetics, ^{18}F-**1** and ^{18}F-**3** were deemed unsuitable for PET neuroimaging of S1R in humans and therefore not selected for the blocking studies. V_{ND} for ^{18}F-**2** and ^{18}F-**4** was estimated from the occupancy plots and used to calculate BP_{ND}, with 1TC-derived values displayed in Table 3. These values demonstrate higher specific binding signals for ^{18}F-**4** than ^{18}F-**2**. A graphical comparison of V_T as a relative measure of BP_{ND} (*27*) revealed a BP_{ND} rank order of ^{18}F-**3** > ^{18}F-**1** > ^{18}F-**4** > ^{18}F-**2**, further supporting the results derived from the blocking studies. The higher BP_{ND} values for ^{18}F-**1** and ^{18}F-**3** than ^{18}F-**2** and ^{18}F-**4** are likely due to their lower K_i values (i.e., higher S1R binding affinity), but higher affinity also contributes to slow and unfavorable binding kinetics in this instance. A comparison of the relative dissociation constants at equilibrium (K_D) yielded a K_D rank order of ^{18}F-**4** > ^{18}F-**2** > ^{18}F-**1** > ^{18}F-**3**, which in general is consistent with in vitro K_i measurements (i.e., K_i values for ^{18}F-**4** and ^{18}F-**2** are higher than those for ^{18}F-**1** and ^{18}F-**3**), but also reveals some differences between in vivo K_D and in vitro K_i values (Table 1). In addition to species-specific variation, these differences between in vitro and in vivo affinities could be due to interlaboratory variations in methodologies and techniques, or temperature effects, because in vitro K_i measurements were performed at room temperature, whereas in vivo measurements were at body temperature (37°C). It should be noted, however, that this method of graphical comparison is less useful for ^{18}F-**1** and ^{18}F-**3** because they display nearly irreversible kinetics.

The irreversible nature of binding for ^{18}F-**1** was confirmed in an in vitro experiment to measure the individual rate constants (k_{on}, k_{off}) and the K_D for ^{18}F-**1** and ^{18}F-**2**, which generated a K_D value of 0.099 nM for ^{18}F-**2** on cloned human S1R and k_{on} and k_{off} values of $3.46 \times 10\ M^{-1}min^{-1}$ and $0.0342\ min^{-1}$, respectively. However, for ^{18}F-**1**, k_{off} was extremely slow and could not be reliably measured (Supplemental Figs. 6 and 7; Supplemental Table 1).

^{18}F-**2** and ^{18}F-**4** may offer advantages over previously developed S1R PET tracers. ^{11}C-SA4503 has been studied in rhesus monkeys (*12,29*), showing high uptake and regional distribution similar to ^{18}F-**2** and ^{18}F-**4** and with reasonable subtype selectivity for S1R (S1R/ S2R = 103). However, it demonstrates slow washout for the time scale of a ^{11}C-labeled PET tracer (*32*) and requires an on-site cyclotron for production. Subsequent studies (*33–35*) with ^{11}C-SA4503 found lower subtype selectivity (S1R/ S2R = 13.3–55.0) than previously reported, and when combined with its affinity for VAChT (K_i = 50 nM, $K_{i\ VAChT}/K_{i\ S1R}$ = 11.3) (*34*), it may exhibit greater nonspecific binding than ^{18}F-**2** and ^{18}F-**4**. A more recent S1R tracer, ^{18}F-FTC-146, has been evaluated in mice, rats, and squirrel monkeys (*36,37*). It demonstrated high binding specificity and selectivity (K_i of 0.0025, 364, and 463 nM, respectively, for S1R, S2R, and VAChT) as well as favorable kinetics and promising imaging properties in the squirrel monkey brain (*36*). Nonetheless, ^{18}F-FTC-146 was also found to have skull uptake in squirrel monkeys, potentially confounding PET quantitation in the brain and thus limiting its utility (*36*). Defluorination and bone uptake of many ^{18}F-labeled tracers

TABLE 3
1TC-Derived BP_{ND} Values of ^{18}F-**2** and ^{18}F-**4** Across Different Brain Regions

	BP_{ND}									
Radioligand	Amygdala	Caudate	Cerebellum	Cingulate cortex	Frontal cortex	Hippocampus	Occipital cortex	Putamen	Temporal cortex	Thalamus
^{18}F-**2**	1.13	0.96	0.98	1.85	1.59	1.38	1.13	1.17	1.40	0.77
^{18}F-**4**	3.76	2.94	2.78	5.21	3.99	4.16	3.09	3.08	3.76	2.78

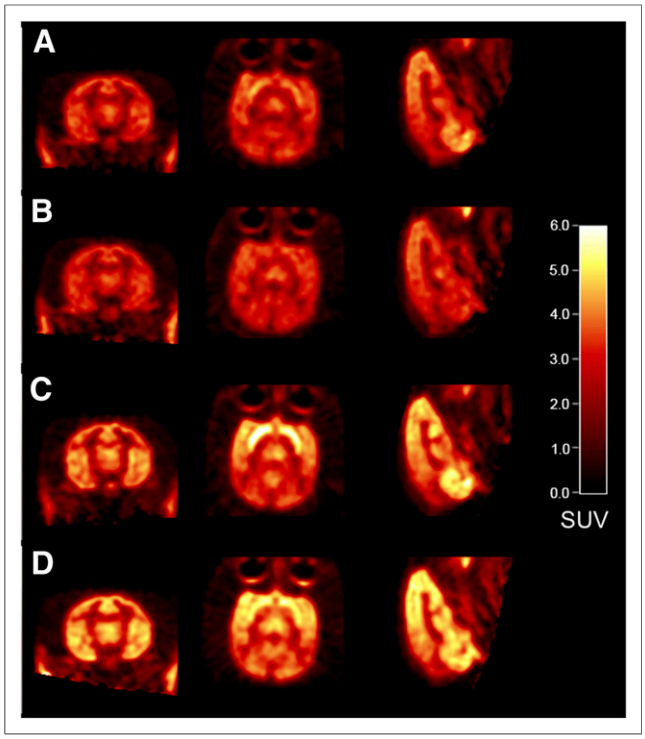

FIGURE 6. PET images (coronal, transverse, and sagittal views) summed from 30 to 45 min of baseline scans for ^{18}F-**1** (A), ^{18}F-**2** (B), ^{18}F-**3** (C), and ^{18}F-**4** (D).

may occur in lower species but not in humans (*38*), so further studies are warranted for ^{18}F-FTC-146. Defluorination was not observed for ^{18}F-**2** and ^{18}F-**4**. Alongside these possible advantages over previously reported S1R tracers, ^{18}F-**2** and ^{18}F-**4** display fast kinetics and high regional BP_{ND} values, the requisite PET imaging characteristics to image and quantitate S1R in the primate brain.

CONCLUSION

In this report, we compare the binding and kinetic properties of 4 ^{18}F-labeled spirocyclic piperidine derivatives in nonhuman primates. Among these tracers, ^{18}F-**2** and ^{18}F-**4** exhibit favorable metabolic profiles, fast brain uptake kinetics, and high specific binding signals in rhesus monkeys. Tracer ^{18}F-**4** has 10-fold-higher f_P, 3-fold-higher BP_{ND}, and greater V_T values than ^{18}F-**2** when compared in the same monkey. Both tracers also give reliable V_T estimates with short (90 min) scan times. Taken together, these results indicate that tracers ^{18}F-**2** and ^{18}F-**4** possess the requisite kinetic and imaging properties as viable PET tracers for imaging S1R in the primate brain, and thus warrant further evaluation in humans.

DISCLOSURE

No potential conflict of interest relevant to this article was reported.

ACKNOWLEDGMENT

We thank the staff at the Yale PET Center for their expert technical assistance.

REFERENCES

1. Crottès D, Guizouarn H, Martin P, Borgese F, Soriani O. The sigma-1 receptor: a regulator of cancer cell electrical plasticity? *Front Physiol.* 2013;4:175.
2. Maurice T, Su T-P. The pharmacology of sigma-1 receptors. *Pharmacol Ther.* 2009;124:195–206.
3. Hayashi T, Su T-P. Sigma-1 receptors at galactosylceramide-enriched lipid microdomains regulate oligodendrocyte differentiation. *Proc Natl Acad Sci USA.* 2004;101:14949–14954.
4. Matsumoto RR, Liu Y, Lerner M, Howard EW, Brackett DJ. Sigma receptors: potential medications development target for anti-cocaine agents. *Eur J Pharmacol.* 2003;469:1–12.
5. Maurice T, Lockhart BP. Neuroprotective and anti-amnesic potentials of sigma (σ) receptor ligands. *Prog Neuropsychopharmacol Biol Psychiatry.* 1997;21:69–102.
6. Matsuno K, Nakazawa M, Okamoto K, Kawashima Y, Mita S. Binding properties of SA4503, a novel and selective σ_1 receptor agonist. *Eur J Pharmacol.* 1996;306:271–279.
7. Tam SW, Cook L. Sigma opiates and certain antipsychotic drugs mutually inhibit (+)-[^{3}H]SKF 10,047 and [^{3}H]haloperidol binding in guinea pig brain membranes. *Proc Natl Acad Sci USA.* 1984;81:5618–5621.
8. Urani A, Privat A, Maurice T. The modulation by neurosteroids of the scopolamine-induced learning impairment in mice involves an interaction with sigma$_1$ (σ_1) receptors. *Brain Res.* 1998;799:64–77.
9. Maurice T, Su TP, Privat A. Sigma$_1$ (σ_1) receptor agonists and neurosteroids attenuate B25-35-amyloid peptide-induced amnesia in mice through a common mechanism. *Neuroscience.* 1998;83:413–428.
10. Collier TL, O'Brien JC, Waterhouse RN. Synthesis of [^{18}F]-1-(3-fluoropropyl)-4-(4-cyanohenoxymethyl)-piperidine: a potential sigma-1 receptor radioligand for PET. *J Labelled Comp Radiopharm.* 1996;38:785–794.
11. Shiue CY, Shiue GG, Zhang SX, et al. *N*-(*N*-benzylpiperidin-4-yl)-2-[^{18}F]fluorobenzamide: a potential ligand for PET imaging of sigma receptors. *Nucl Med Biol.* 1997;24:671–676.
12. Kawamura K, Ishiwata K, Tajima H, et al. In vivo evaluation of [^{11}C]SA4503 as a PET ligand for mapping CNS sigma$_1$ receptors. *Nucl Med Biol.* 2000;27:255–261.
13. James ML, Shen B, Zavaleta CL, et al. New positron emission tomography (PET) radioligand for imaging sigma-1 receptors in living subjects. *J Med Chem.* 2012;55:8272–8282.
14. Li Y, Wang X, Zhang J, et al. Synthesis and evaluation of novel ^{18}F-labeled spirocyclic piperidine derivatives as σ_1 receptor ligands for positron emission tomography imaging. *J Med Chem.* 2013;56:3478–3491.
15. Holl K, Falck E, Kohler J, et al. Synthesis, characterization, and metabolism studies of fluspidine enantiomers. *ChemMedChem.* 2013;8:2047–2056.
16. Fischer S, Wiese C, Maestrup EG, et al. Molecular imaging of sigma receptors: synthesis and evaluation of the potent σ_1 selective radioligand [^{18}F]fluspidine. *Eur J Nucl Med Mol Imaging.* 2011;38:540–551.
17. Brust P, Deuther-Conrad W, Becker G, et al. Distinctive in vivo kinetics of the new σ_1 receptor ligands (R)-(+)- and (S)-(-)-^{18}F-fluspidine in porcine brain. *J Nucl Med.* 2014;55:1730–1736.
18. Kranz M, Sattler B, Wüst N, et al. Evaluation of the enantiomer specific biokinetics and radiation doses of [^{18}F]fluspidine: a new tracer in clinical translation for imaging of σ_1 receptors. *Molecules.* 2016;21:1164.
19. Chen Y-Y, Wang X, Zhang J-M, et al. Synthesis and evaluation of a ^{18}F-labeled spirocyclic piperidine derivative as promising σ_1 receptor imaging agent. *Bioorg Med Chem.* 2014;22:5270–5278.
20. Zheng MQ, Nabulsi N, Kim SJ, et al. Synthesis and evaluation of ^{11}C-LY2795050 as a kappa-opioid receptor antagonist radiotracer for PET imaging. *J Nucl Med.* 2013;54:455–463.
21. Bois F, Gallezot JD, Zheng MQ, et al. Evaluation of [^{18}F]-(-)-norchlorofluorohomoepibatidine ([^{18}F]-(-)-NCFHEB) as a PET radioligand to image the nicotinic acetylcholine receptors in non-human primates. *Nucl Med Biol.* 2015;42:570–577.
22. Schoultz BW, Hjornevik T, Reed BJ, et al. Synthesis and evaluation of three structurally related ^{18}F-labeled orvinols of different intrinsic activities: 6-*O*-[^{18}F]fluoroethyl-diprenorphine ([^{18}F]FDPN), 6-*O*-[^{18}F]fluoroethyl-buprenorphine ([^{18}F]FBPN), and 6-*O*-[^{18}F]fluoroethyl-phenethyl-orvinol ([^{18}F]FPEO). *J Med Chem.* 2014;57:5464–5469.
23. Hilton J, Yokoi F, Dannals RF, Ravert HT, Szabo Z, Wong DF. Column-switching HPLC for the analysis of plasma in PET imaging studies. *Nucl Med Biol.* 2000;27:627–630.
24. Wilson AA, Jin L, Garcia A, DaSilva JN, Houle S. An admonition when measuring the lipophilicity of radiotracers using counting techniques. *Appl Radiat Isot.* 2001;54:203–208.

25. Ichise M, Toyama H, Innis RB, Carson RE. Strategies to improve neuroreceptor parameter estimation by linear regression analysis. *J Cereb Blood Flow Metab.* 2002;22:1271–1281.
26. Innis RB, Cunningham VJ, Delforge J, et al. Consensus nomenclature for *in vivo* imaging of reversibly binding radioligands. *J Cereb Blood Flow Metab.* 2007;27: 1533–1539.
27. Guo Q, Owen DR, Rabiner EA, Turkheimer FE, Gunn RN. A graphical method to compare the *in vivo* binding potential of PET radioligands in the absence of a reference region: application to [^{11}C]PBR28 and [^{18}F] PBR111 for TSPO imaging. *J Cereb Blood Flow Metab.* 2014;34:1162–1168.
28. Cunningham VJ, Rabiner EA, Slifstein M, Laruelle M, Gunn RN. Measuring drug occupancy in the absence of a reference region: the Lassen plot re-visited. *J Cereb Blood Flow Metab.* 2010;30:46–50.
29. Kawamura K, Kimura Y, Tsukada H, et al. An increase of sigma receptors in the aged monkey brain. *Neurobiol Aging.* 2003;24:745–752.
30. Mash DC, Zabetian CP. Sigma receptors are associated with cortical limbic areas in the primate brain. *Synapse.* 1992;12:195–205.
31. Sakata M, Kimura Y, Naganawa M, et al. Mapping of human cerebral sigma$_1$ receptors using positron emission tomography and [^{11}C]SA4503. *Neuroimage.* 2007;35:1–8.
32. Sakata M, Kimura Y, Naganawa M, et al. Shortened protocol in practical [^{11}C] SA4503-PET studies for sigma$_1$ receptor quantification. *Ann Nucl Med.* 2008;22:143–146.
33. Lever JR, Gustafson JL, Xu R, Allmon RL, Lever SZ. σ_1 and σ_2 receptor binding affinity and selectivity of SA4503 and fluoroethyl SA4503. *Synapse.* 2006;59:350–358.
34. Ishiwata K, Kawamura K, Yajima K, QingGeLeTu, Mori H, Shiba K. Evaluation of (+)-*p*-[^{11}C]methylvesamicol for mapping sigma1 receptors: a comparison with [^{11}C]SA4503. *Nucl Med Biol.* 2006;33:543–548.
35. Hirata M, Mori T, Soga S, Umeda T, Ohmomo Y. Synthesis and *in vitro* evaluation of iodinated derivatives of piperazine as a new ligand for sigma receptor imaging by single photon emission computed tomography. *Chem Pharm Bull (Tokyo).* 2006;54:470–475.
36. James ML, Shen B, Nielsen CH, et al. Evaluation of σ_1 receptor radioligand ^{18}F-FTC-146 in rats and squirrel monkeys using PET. *J Nucl Med.* 2014;55:147–153.
37. Shen B, James ML, Andrews L, et al. Further validation to support clinical translation of [^{18}F]FTC-146 for imaging sigma-1 receptors. *EJNMMI Res.* 2015;5:49.
38. Pike VW. PET radiotracers: crossing the blood–brain barrier and surviving metabolism. *Trends Pharmacol Sci.* 2009;30:431–440.